

# An Efficient Planar Bundle Adjustment Algorithm

Lipu Zhou\*  
Magic Leap

Daniel Koppel†  
Magic Leap

Hui Ju‡  
Magic Leap

Frank Steinbruecker§  
Magic Leap

Michael Kaess¶  
Carnegie Mellon University

## ABSTRACT

This paper presents an efficient algorithm for the least-squares problem using the point-to-plane cost, which aims to jointly optimize depth sensor poses and plane parameters for 3D reconstruction. We call this least-squares problem **Planar Bundle Adjustment (PBA)**, due to the similarity between this problem and the original Bundle Adjustment (BA) in visual reconstruction. As planes ubiquitously exist in the man-made environment, they are generally used as landmarks in SLAM algorithms for various depth sensors. PBA is important to reduce drift and improve the quality of the map. However, directly adopting the well-established BA framework in visual reconstruction will result in a very inefficient solution for PBA. This is because a 3D point only has one observation at a camera pose. In contrast, a depth sensor can record hundreds of points in a plane at a time, which results in a very large nonlinear least-squares problem even for a small-scale space. The main contribution of this paper is an efficient solution for the PBA problem using the point-to-plane cost. We introduce a reduced Jacobian matrix and a reduced residual vector, and prove that they can replace the original Jacobian matrix and residual vector in the generally adopted Levenberg-Marquardt (LM) algorithm. This significantly reduces the computational cost. Besides, when planes are combined with other features for 3D reconstruction, the reduced Jacobian matrix and residual vector can also replace the corresponding parts derived from planes. Our experimental results show that our algorithm can significantly reduce the computational time compared to the solution using the traditional BA framework. In addition, our algorithm is faster, more accurate, and more robust to initialization errors compared to the start-of-the-art solution using the plane-to-plane cost [3].

**Index Terms:** Bundle Adjustment—Nonlinear Optimization—SLAM—Depth Sensor

## 1 INTRODUCTION

Simultaneous localization and mapping (SLAM) is important for Augmented Reality (AR) systems, and many other computer vision and robotics applications. Generally, visual SLAM algorithms [15, 19, 20, 23, 30] yield sparse or semi-dense maps. It is difficult for visual SLAM algorithms to recover the structure of textureless areas, such as white walls. Recently, depth sensors have become available for AR glasses and smart phones. This has made possible the building of dense 3D maps in real time [9–12, 28], which is desirable, not only for providing the necessary information for localization, but also the information for environment understanding, such as 3D object classification and semantic segmentation [27], required in most of today’s AR applications. As planes ubiquitously exist in man-made scenes, they are generally exploited as features in SLAM algorithms for various depth sensors [9–12, 14, 16, 25, 28, 32, 36, 37, 40]. In recent

work [18], planes are also used in a novel Visual-Inertial Odometry (VIO) system. In addition, planes are important locations for an AR system to display virtual information as demonstrated in [28]. Thus planes play an important role in AR applications. This paper focuses on optimizing the plane model of an environment.

It is known that bundle adjustment (BA) is crucial for visual reconstruction to generate a high quality and globally consistent 3D map. Thus BA has been extensively investigated in the literature [2, 6, 7, 13, 19, 21, 29, 33, 35, 39, 41]. Analogously to the visual reconstruction case, we face a nonlinear least-squares problem whose goal is to obtain optimal poses and plane parameters for depth data. Here we name this least-squares problem as **Planar Bundle Adjustment (PBA)**, due to the similarity between this least-squares problem and BA. Although BA for visual reconstruction has been well studied in the literature, little research has been done on the PBA. Thus, this raises the demand for studying the PBA problem for depth sensors.

The PBA is the problem of jointly optimizing parameters of planes and sensor poses. Although the plane is seemingly the counterpart of the point in BA for visual reconstruction, there exists a significant difference between them. In the literature, the plane-to-plane distance based on the rigid-body transformation for plane parameters is generally employed to construct the cost function. However, this cost function may introduce bias which may result in a suboptimal solution as described in Sect. 2. Thus this paper adopts the point-to-plane distance to construct the cost function. A 3D point can only yield one observation for each camera pose. However, as a plane is an infinite object, one recording of a depth sensor can provide many points as a partial observation of a plane. Thus a single depth sensor recording can generate many constraints on planes and poses. Therefore, directly adopting the original visual BA framework to the planar case will result in a large-scale nonlinear least-square problem even for a small scene, which incurs high computational cost and memory consumption. This paper addresses this problem.

The main contribution of this paper is an efficient planar bundle adjustment algorithm. The key point of our algorithm is to explore the special structure of PBA. Based on the special structure of PBA, we introduce a reduced Jacobian matrix and a reduced residual vector. We prove that no matter how many points of a plane are recorded by a depth sensor, the derived Jacobian matrix and residual vector can be replaced by the reduced ones in the Levenberg-Marquardt (LM) algorithm [17, 22]. The reduced Jacobian matrix and residual vector have fixed sizes that are much smaller than the original ones. This significantly reduces computational cost and memory usage. More generally, when 3D reconstruction applications exploit planes together with other features such as points [5, 8, 31, 34, 38], the same reduction technique can be applied to the blocks inside the Jacobian and the residual, which correspond to the planar constraints.

## 2 RELATED WORK AND THEORETICAL BACKGROUND

Planes are widely adopted as landmarks in SLAM algorithms for depth sensors. The related topics include plane detection, matching, 3D registration and joint optimization with poses and planes, *etc.* The research on the joint optimization problem is relative small. This paper focuses on this problem. In this section, we introduce the related work and the theoretical background for the optimization problem. In the following description, we use italic, boldfaced lowercase and boldfaced uppercase letters to represent scalars, vectors

\*e-mail: lzhou@magicleap.com

†e-mail: dkoppel@magicleap.com

‡e-mail: hju@magicleap.com

§e-mail: steinbruecker@magicleap.com

¶e-mail: kaess@cmu.edu

and matrices, respectively.

## 2.1 Cost Functions for the Plane Correspondence

One requisite step of formulating an optimization problem is to construct the cost function. For the plane correspondence, there are two cost functions generally used in the literature, *i.e.*, **plane-to-plane** and **point-to-plane**.

**Plane-to-plane cost** is based on the rigid-body transformation for the plane parameters. Specifically, suppose a plane is represented by the Hesse normal form as  $\boldsymbol{\pi} = [\mathbf{n}; d]$ , where  $\mathbf{n}$  is the plane normal with  $\|\mathbf{n}\|_2 = 1$  and  $d$  is the negative distance from the coordinate system origin to the plane. Assume the rotation and translation from a depth sensor's local coordinate system to a global coordinate system are  $\mathbf{R}$  and  $\mathbf{t}$ , respectively. Let  $\boldsymbol{\pi}_s$  represent the parameters of a plane in the depth sensor coordinate system, which are estimated from a set of points  $\mathbb{P}$  in the depth sensor measurements, and  $\boldsymbol{\pi}_g$  denote the same plane's parameters in the global coordinate system. Then the relation between  $\boldsymbol{\pi}_s$  and  $\boldsymbol{\pi}_g$  can be described as [7]

$$\boldsymbol{\pi}_s = \mathbf{T}^T \boldsymbol{\pi}_g, \quad \mathbf{T} = \begin{bmatrix} \mathbf{R} & \mathbf{t} \\ \mathbf{0} & 1 \end{bmatrix}. \quad (1)$$

$\boldsymbol{\pi}_g$  and  $\mathbf{T}$  are the variables that we want to estimate. We can have a general form of the plane-to-plane residual as below

$$\boldsymbol{\pi}_s \ominus \mathbf{T}^T \boldsymbol{\pi}_g, \quad (2)$$

where  $\ominus$  is a function to measure the difference between  $\boldsymbol{\pi}_s$  and  $\mathbf{T}^T \boldsymbol{\pi}_g$ . Kaess [12] represents planes as quaternions, and defines  $\ominus$  by measuring the difference between two quaternions. Geneva *et al.* [3] introduce the closest point (CP) vector, *i.e.*  $d\mathbf{n}$ , to parameterize a plane. They define  $\ominus$  as the difference between two CP vectors.

The above equation (2) can be directly used to construct cost function for jointly tuning poses and planes [11]. But the relative plane formulation introduced by Kaess [12] converges faster. In the relative plane formulation, a plane is expressed relative to the first pose that observes it. This formulation is adopted later in [9, 10] for global joint optimization of poses and planes when loop closure occurs. Geneva *et al.* [3] present a similar relative plane formulation as [12]. They introduce the CP vector to represent the plane, which shows improved accuracy and faster convergence compared to the plane parameterization using quaternion introduced in [12].

**Point-to-plane cost** is the squared distance from a point to a plane. As mentioned above,  $\mathbb{P}$  is the point set of a plane observed by a depth sensor. Assume  $\mathbf{p}_i \in \mathbb{P}$  and  $\boldsymbol{\pi}_g = [\mathbf{n}_g; d_g]$ . The signed distance from  $\mathbf{p}_i$  to  $\boldsymbol{\pi}_g$  has the form as

$$\delta = \mathbf{n}_g \cdot (\mathbf{R}\mathbf{p}_i + \mathbf{t}) + d_g, \quad (3)$$

where  $\cdot$  represents the dot product. The point-to-plane cost  $\delta^2$  is generally employed to calculate the pose between a local depth sensor point cloud and a global point cloud [10, 24, 40, 43] rather than to jointly optimize poses and plane parameters. This is because there generally exists a large number of points in  $\mathbb{P}$ , which leads to a very large-scale least-squares problem, if this particular cost function is used. Thus, it is seldom adopted in the SLAM algorithm for global poses and planes joint optimization.

**plane-to-plane vs. point-to-plane** As described in [7], the cost function will impact the accuracy of the solution. The point-to-plane cost is well defined. It is the squared distance from  $\mathbf{p}_i$  to  $\boldsymbol{\pi}_g$ , which is invariant to rigid transformations. This means the cost is invariant to the choice of the global coordinate system. It only depends on estimation errors of poses and planes. However, the plane-to-plane cost based on plane parameter transformation (1) does not have this property. As demonstrated in Fig. 1(a) changing the coordinate system will vary the plane-to-plane cost. Thus the accuracy of the result of minimizing the plane-to-plane cost

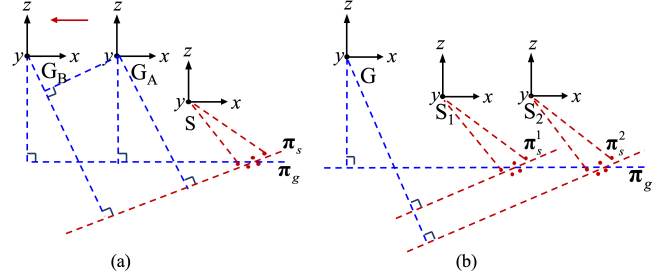


Figure 1: A schematic illustrating the potential problems of the plane-to-plane cost. (a) Plane-to-plane cost is not invariant to rigid transformations. When the coordinate system shifts from  $G_A$  to  $G_B$ , the plane-to-plane cost for  $\boldsymbol{\pi}_s \leftrightarrow \boldsymbol{\pi}_g$  changes. However, the point-to-plane cost is invariant. (b) Plane-to-plane cost may introduce bias. The two point clouds acquired from the global plane  $\boldsymbol{\pi}_g$  at two poses ( $S_1$  and  $S_2$ ) have the same noise level. Their sums of squared distances to  $\boldsymbol{\pi}_g$  are the same. Thus they have the same point-to-plane cost. However, the plane-to-plane costs for  $\boldsymbol{\pi}_s^1 \leftrightarrow \boldsymbol{\pi}_g$  and  $\boldsymbol{\pi}_s^2 \leftrightarrow \boldsymbol{\pi}_g$  are different, as  $\boldsymbol{\pi}_s^1$  and  $\boldsymbol{\pi}_s^2$  have different parameters. If we consider the CP vector difference [3],  $\boldsymbol{\pi}_s^1$  will yield a smaller cost. This may cause the optimization algorithm to change the second pose to push  $\boldsymbol{\pi}_s^2$  toward  $\boldsymbol{\pi}_s^1$  to reduce the plane-to-plane cost. This bias may result in less accurate results.

may depend on the particular choice of coordinate systems, which introduces uncertainty to the solution.

Furthermore, the plane-to-plane cost may introduce bias. For example, given the ground truth of the two poses and  $\boldsymbol{\pi}_g$ , the two local point clouds in Fig. 1(b) generate different plane-to-plane costs, although they yield the same point-to-plane costs. Plane  $\boldsymbol{\pi}_s^1$  has smaller cost than  $\boldsymbol{\pi}_s^2$  merely because of the certain choice of the global coordinate system rather than the second pose error is larger. However, as plane  $\boldsymbol{\pi}_s^1$  generates smaller cost than  $\boldsymbol{\pi}_s^2$ , this may cause the optimization algorithm to change the second pose of the sensor to push plane  $\boldsymbol{\pi}_s^2$  toward plane  $\boldsymbol{\pi}_s^1$  to minimize the plane-to-plane cost, which is prone to increase errors.

Our experimental results show that minimizing the point-to-plane cost results in a more accurate solution than minimizing the plane-to-plane cost. In addition, our results show that the point-to-plane cost is more robust to initialization errors. However, using the point-to-plane cost yields a much larger scale least-squares problem. This paper presents an efficient solution to address this problem.

## 2.2 The Bundle Adjustment Problem

3D reconstruction is a fundamental problem with a large number of applications. BA is a crucial step for 3D reconstruction. Let us first consider the well-established BA framework for visual reconstruction.

The BA framework for visual reconstruction is essentially a non-linear least-squares problem with sparse structure [2, 19, 21, 33, 35]. The LM algorithm [17, 22] is generally adopted to solve this problem. Let us begin with a brief introduction of the LM algorithm for a general least-squares problem.

Suppose that we have an  $n$ -dimensional measurements  $\mathbf{y} = [y_1; y_2; \dots; y_n]$  modeled by function  $\mathbf{f}(\mathbf{x}) = [f_1(\mathbf{x}); f_2(\mathbf{x}); \dots; f_n(\mathbf{x})]$ , where  $\mathbf{x} \in \mathbb{R}^m$  is an  $m$ -dimensional model parameter vector which we seek to estimate. The least-squares problem is to find the optimal  $\hat{\mathbf{x}}$  which minimizes the sum of squared errors of  $\boldsymbol{\delta}(\mathbf{x}) = \mathbf{f}(\mathbf{x}) - \mathbf{y}$ , *i.e.*,

$$\hat{\mathbf{x}} = \arg \min_{\mathbf{x}} \frac{1}{2} \|\boldsymbol{\delta}(\mathbf{x})\|_2^2. \quad (4)$$

We use  $\mathbf{J}(\mathbf{x})$  to represent the Jacobian matrix of  $\mathbf{f}(\mathbf{x})$  at  $\mathbf{x}$ , whose  $i$ th row and  $j$ th column element is  $J_{ij}(\mathbf{x}) = \frac{\partial f_i(\mathbf{x})}{\partial x_j}$ , where  $x_j$  is the

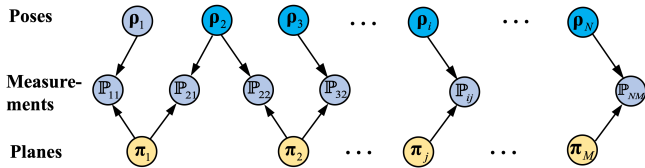


Figure 2: Bayes Net of PBA with  $N$  poses and  $M$  planes. The first pose  $\rho_1$  is fixed during the optimization.  $\mathbb{P}_{ij}$  is the set of measurements of the  $j$ th plane  $\pi_j$  recorded at the  $i$ th pose  $\rho_i$ . PBA is the problem of jointly refining  $\rho_i$  ( $i \neq 1$ ) and  $\pi_j$ .

$j$ th element of  $\mathbf{x}$ . To keep the expression simple in the following description, we only use the name of the function and do not explicitly include the variable of the function unless necessary.

Given an initial estimation of the model parameters, the LM algorithm iteratively refines the solution. At each iteration, the LM algorithm calculates the step  $\xi$  by solving the following linear system

$$(\mathbf{J}^T \mathbf{J} + \lambda \mathbf{I}) \xi = -\mathbf{J}^T \delta, \quad (5)$$

where  $\mathbf{I}$  denotes an  $m \times m$  identity matrix and  $\lambda$  is a scalar that is adjusted at each iteration to ensure that  $\xi$  leads to a reduced cost. After we solve the linear system (5),  $\mathbf{x}$  is updated by  $\mathbf{x} \leftarrow \mathbf{x} + \xi$ .

As mentioned above, the BA for visual reconstruction is a nonlinear least-squares problem. It refines camera poses  $\mathbf{x}_c$  and 3D point coordinates  $\mathbf{x}_p$  to minimize the sum of squared re-projection errors. Typically, the model parameters are organized as  $\mathbf{x} = [\mathbf{x}_c; \mathbf{x}_p]$ . Thus, the Jacobian matrix can be divided as  $\mathbf{J} = [\mathbf{J}_c; \mathbf{J}_p]$ . According to this structure, the equation system (5) can be rewritten as

$$\begin{bmatrix} \mathbf{A} & \mathbf{W} \\ \mathbf{W}^T & \mathbf{B} \end{bmatrix} \begin{bmatrix} \xi_c \\ \xi_p \end{bmatrix} = - \begin{bmatrix} \mathbf{J}_c^T \delta \\ \mathbf{J}_p^T \delta \end{bmatrix}, \quad (6)$$

where  $\mathbf{A} = \mathbf{J}_c^T \mathbf{J}_c + \lambda_c \mathbf{I}$ ,  $\mathbf{B} = \mathbf{J}_p^T \mathbf{J}_p + \lambda_p \mathbf{I}$  and  $\mathbf{W} = \mathbf{J}_c^T \mathbf{J}_p$ .  $\mathbf{A}$  and  $\mathbf{B}$  are usually block diagonal matrices. The Schur complement trick is generally adopted to solve this sparse linear system [33].

The planar BA problem yields a similar structure as (6). But we cannot directly adopt the above method. This is because one plane can generate many observations in one depth sensor recording, which can make the size of the resulting nonlinear least-squares problem prohibitively large. It would be time-consuming to just compute the Jacobian matrix  $\mathbf{J}$  and the residual  $\delta$ , not to mention to construct and solve the linear system (6). This paper shows that  $\mathbf{J}$  of PBA has a special structure, which can be used to significantly reduce the computational cost.

### 3 PLANAR BUNDLE ADJUSTMENT

In this section, we elaborate our solution for the PBA problem. We begin with the formulation of the PBA problem. We then present our solution for this problem.

#### 3.1 Problem Formulation

Fig. 2 presents the Bayes Net of a PBA problem. We assume that there are  $M$  planes and  $N$  sensor poses. Denote the rotation and translation of the  $i$ th pose as  $\mathbf{R}_i \in SO_3$  and  $\mathbf{t}_i \in \mathbb{R}^3$ , respectively. Suppose the  $j$ th plane has the parameters  $\pi_j = [\mathbf{n}_j; d_j]$ . The measurements of the  $j$ th plane at the  $i$ th pose are a set of  $K_{ij}$  points defined as:

$$\mathbb{P}_{ij} = \{\mathbf{p}_{ijk}\}_{k=1}^{K_{ij}} \quad (7)$$

Each  $\mathbf{p}_{ijk} \in \mathbb{P}_{ij}$  provides one constraint on the  $i$ th pose and  $j$ th plane, which is demonstrated in Fig. 3. The residual  $\delta_{ijk}$  is the signed distance from  $\mathbf{p}_{ijk}$  to plane  $\pi_j$  which can be written as

$$\delta_{ijk} = \mathbf{n}_j \cdot (\mathbf{R}_i \mathbf{p}_{ijk} + \mathbf{t}_i) + d_j, \quad (8)$$

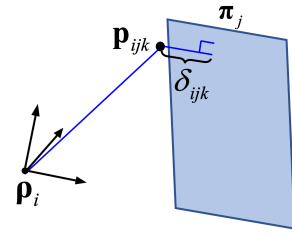


Figure 3: The geometric entities involved in PBA.  $\mathbf{p}_{ijk}$  is the  $k$ th point of the point set  $\mathbb{P}_{ij}$  that are captured from the  $j$ th plane  $\pi_j$  at the  $i$ th pose  $\rho_i$ .  $\delta_{ijk}$  is the signed distance from  $\mathbf{p}_{ijk}$  to  $\pi_j$  defined in (8).

Unlike  $\mathbf{t}_i$ , the rotation  $\mathbf{R}_i$  and plane parameters  $\pi_j$  have extra constraints. The parameterization of both entities has been well-studied. For instance,  $\mathbf{R}_i$  can be parameterized by a quaternion, angle-axis or Euler angles. The plane parameters  $\pi_j$  can be represented by homogeneous coordinates [7], closest point parameterization [38] or the minimal parameterization based on quaternion introduced in [12]. Our algorithm does not depend on a special parameterization. We define  $\theta_i \mapsto \mathbf{R}(\theta_i)$  and  $\omega_j \mapsto \pi(\omega_j)$  to represent arbitrary parameterization for rotation and plane parameters.  $\theta_i$  and  $\mathbf{t}_i$  are related to the sensor pose. According to the convention of visual BA introduced above, we combine them as  $\rho_i = [\theta_i; \mathbf{t}_i]$ . Generally,  $\rho_i$  has 6 or 7 unknowns, depending on the parameterization of the rotation matrix (6 for the cases of any minimal representations of the rotation and 7 for the quaternion).  $\omega_j$  generally has 3 or 4 unknowns (3 for minimal representations of a plane [12, 38] and 4 for the homogeneous coordinates of a plane [7]).

Using the above notations,  $\delta_{ijk}$  is a function of  $\rho_i$  and  $\omega_j$ . The PBA is the problem of jointly refining all  $\rho_i$  ( $i \neq 1$ ) and  $\omega_j$  by minimizing the following nonlinear least-squares problem

$$\min_{\rho_i, \omega_j} \sum_{i \neq 1} \sum_j \sum_k \delta_{ijk}^2(\rho_i, \omega_j). \quad (9)$$

Here the first pose  $\rho_1$  is fixed during the optimization to anchor the coordinate system rigidly.

#### 3.2 Structure of the Jacobian Matrix

One crucial step of the LM algorithm is to calculate the Jacobian matrix. The Jacobian matrix of planar BA has a special structure. The observation of the  $j$ th plane at the  $i$ th pose is a point set  $\mathbb{P}_{ij}$ . Let us consider the Jacobian matrix  $\mathbf{J}_{ij}$  derived from  $\mathbb{P}_{ij}$ . The whole Jacobian matrix  $\mathbf{J}$  is the stack of all  $\mathbf{J}_{ij}$ . Assume there are  $K_{ij}$  points in  $\mathbb{P}_{ij}$ .  $\mathbf{J}_{ij}$  ( $i \neq 1$ ) has the following form

$$\mathbf{J}_{ij} = \begin{bmatrix} \mathbf{0} & \dots & \overbrace{\frac{\partial \delta_{ij1}}{\partial \rho_i}} & \dots & \mathbf{0} & \dots & \overbrace{\frac{\partial \delta_{ij1}}{\partial \omega_j}} & \dots & \mathbf{0} \\ \mathbf{0} & \dots & \frac{\partial \delta_{ij2}}{\partial \rho_i} & \dots & \mathbf{0} & \dots & \frac{\partial \delta_{ij2}}{\partial \omega_j} & \dots & \mathbf{0} \\ \vdots & \ddots & \vdots & \ddots & \vdots & \ddots & \vdots & \ddots & \vdots \\ \mathbf{0} & \dots & \frac{\partial \delta_{ijK_{ij}}}{\partial \rho_i} & \dots & \mathbf{0} & \dots & \frac{\partial \delta_{ijK_{ij}}}{\partial \omega_j} & \dots & \mathbf{0} \end{bmatrix} \quad (10)$$

$\underbrace{\hspace{15em}}_{N-1 \text{ pose}} \quad \underbrace{\hspace{15em}}_{M \text{ plane}}$

To calculate  $\frac{\partial \delta_{ijk}}{\partial \rho_i}$  and  $\frac{\partial \delta_{ijk}}{\partial \omega_j}$ , we begin by considering the form of  $\delta_{ijk}$  in (8). Let us define

$$\mathbf{R}_i = \begin{bmatrix} R_i^{1,1} & R_i^{1,2} & R_i^{1,3} \\ R_i^{2,1} & R_i^{2,2} & R_i^{2,3} \\ R_i^{3,1} & R_i^{3,2} & R_i^{3,3} \end{bmatrix}, \mathbf{t}_i = \begin{bmatrix} t_i^1 \\ t_i^2 \\ t_i^3 \end{bmatrix}, \mathbf{n}_j = \begin{bmatrix} n_j^1 \\ n_j^2 \\ n_j^3 \end{bmatrix}, \mathbf{p}_{ijk} = \begin{bmatrix} x_{ijk} \\ y_{ijk} \\ z_{ijk} \end{bmatrix}. \quad (11)$$

Note that the elements of  $\mathbf{R}_i$  defined above are functions of  $\boldsymbol{\theta}_i$ , and also that  $d_j$  and the elements of  $\mathbf{n}_j$  are functions of  $\boldsymbol{\omega}_j$ . Substituting (11) into (8) and expanding it, we have

$$\begin{aligned} \delta_{ijk} = & x_{ijk}R_i^{1,1}n_j^1 + y_{ijk}R_i^{1,2}n_j^2 + z_{ijk}R_i^{1,3}n_j^3 + \\ & x_{ijk}R_i^{2,1}n_j^2 + y_{ijk}R_i^{2,2}n_j^2 + z_{ijk}R_i^{2,3}n_j^2 + \\ & x_{ijk}R_i^{3,1}n_j^3 + y_{ijk}R_i^{3,2}n_j^3 + z_{ijk}R_i^{3,3}n_j^3 + \\ & n_j^1t_i^1 + n_j^2t_i^2 + n_j^3t_i^3 + d_j. \end{aligned} \quad (12)$$

We can rewrite (12) as

$$\delta_{ijk} = \mathbf{c}_{ijk} \cdot \mathbf{v}_{ij}, \quad (13)$$

where  $\mathbf{c}_{ijk}$  and  $\mathbf{v}_{ij}$  are 13-dimensional vectors as

$$\begin{aligned} \mathbf{c}_{ijk} = & [x_{ijk}, y_{ijk}, z_{ijk}, x_{ijk}, y_{ijk}, z_{ijk}, x_{ijk}, y_{ijk}, z_{ijk}, 1, 1, 1, 1]^T, \\ \mathbf{v}_{ij} = & [R_i^{1,1}n_j^1, R_i^{1,2}n_j^1, R_i^{1,3}n_j^1, R_i^{2,1}n_j^2, R_i^{2,2}n_j^2, R_i^{2,3}n_j^2, R_i^{3,1}n_j^3, \\ & R_i^{3,2}n_j^3, R_i^{3,3}n_j^3, n_j^1t_i^1, n_j^2t_i^2, n_j^3t_i^3, d_j]^T. \end{aligned} \quad (14)$$

The elements in  $\mathbf{c}_{ijk}$  are from the observation  $\mathbf{p}_{ijk}$  or 1. They are constants. On the other hand, the elements in  $\mathbf{v}_{ij}$  are functions of  $\boldsymbol{\rho}_i$  and  $\boldsymbol{\omega}_j$ . They are related to the unknowns which we want to estimate.

Let us calculate the partial derivative of  $\delta_{ijk}$ . Assume that  $\boldsymbol{\rho}_i$  has  $n_{\boldsymbol{\rho}}$  unknowns and  $\boldsymbol{\omega}_j$  has  $n_{\boldsymbol{\omega}}$  unknowns. We define

$$\boldsymbol{\zeta}_{ij} = \begin{Bmatrix} \boldsymbol{\rho}_i \\ \boldsymbol{\omega}_j \end{Bmatrix} \begin{matrix} n_{\boldsymbol{\rho}} \text{ unknowns} \\ n_{\boldsymbol{\omega}} \text{ unknowns} \end{matrix} \quad (15)$$

Suppose  $\zeta_{ij}^d$  is the  $d$ th element of  $\boldsymbol{\zeta}_{ij}$ . According to (13), the partial derivative of  $\delta_{ijk}$  with respect to  $\zeta_{ij}^d$  has the following form

$$\frac{\partial \delta_{ijk}}{\partial \zeta_{ij}^d} = \frac{\partial \mathbf{c}_{ijk} \cdot \mathbf{v}_{ij}}{\partial \zeta_{ij}^d} = \mathbf{c}_{ijk} \cdot \frac{\partial \mathbf{v}_{ij}}{\partial \zeta_{ij}^d}, \quad (16)$$

where  $\frac{\partial \mathbf{v}_{ij}}{\partial \zeta_{ij}^d}$  is a 13-dimensional vector whose elements are the partial derivatives of the elements of  $\mathbf{v}_{ij}$  with respect to  $\zeta_{ij}^d$ .

Then we consider  $\frac{\partial \delta_{ijk}}{\partial \boldsymbol{\rho}_i}$  and  $\frac{\partial \delta_{ijk}}{\partial \boldsymbol{\omega}_j}$ . According to (16),  $\frac{\partial \delta_{ijk}}{\partial \boldsymbol{\rho}_i}$  has the following form

$$\begin{aligned} \frac{\partial \delta_{ijk}}{\partial \boldsymbol{\rho}_i} &= \left[ \frac{\partial \delta_{ijk}}{\partial \zeta_{ij}^1}, \dots, \frac{\partial \delta_{ijk}}{\partial \zeta_{ij}^{n_{\boldsymbol{\rho}}}} \right] \\ &= \left[ \mathbf{c}_{ijk} \cdot \frac{\partial \mathbf{v}_{ij}}{\partial \zeta_{ij}^1}, \dots, \mathbf{c}_{ijk} \cdot \frac{\partial \mathbf{v}_{ij}}{\partial \zeta_{ij}^{n_{\boldsymbol{\rho}}}} \right] \\ &= \mathbf{c}_{ijk}^T \underbrace{\left[ \frac{\partial \mathbf{v}_{ij}}{\partial \zeta_{ij}^1}, \dots, \frac{\partial \mathbf{v}_{ij}}{\partial \zeta_{ij}^{n_{\boldsymbol{\rho}}}} \right]}_{\mathbf{v}_{ij}^{\boldsymbol{\rho}_i}} = \mathbf{c}_{ijk}^T \mathbf{V}_{ij}^{\boldsymbol{\rho}_i}. \end{aligned} \quad (17)$$

$\mathbf{V}_{ij}^{\boldsymbol{\rho}_i}$  is generally a  $13 \times 6$  or  $13 \times 7$  matrix ( $13 \times 6$  for minimal representations of the rotation matrix and  $13 \times 7$  for quaternion).

Similarly, we can calculate  $\frac{\partial \delta_{ijk}}{\partial \boldsymbol{\omega}_j}$  as

$$\frac{\partial \delta_{ijk}}{\partial \boldsymbol{\omega}_j} = \mathbf{c}_{ijk}^T \underbrace{\left[ \frac{\partial \mathbf{v}_{ij}}{\partial \zeta_{ij}^{n_{\boldsymbol{\rho}}+1}}, \dots, \frac{\partial \mathbf{v}_{ij}}{\partial \zeta_{ij}^{n_{\boldsymbol{\rho}}+n_{\boldsymbol{\omega}}}} \right]}_{\mathbf{v}_{ij}^{\boldsymbol{\omega}_j}} = \mathbf{c}_{ijk}^T \mathbf{V}_{ij}^{\boldsymbol{\omega}_j} \quad (18)$$

Typically,  $\mathbf{V}_{ij}^{\boldsymbol{\omega}_j}$  is a  $13 \times 3$  or  $13 \times 4$  matrix ( $13 \times 3$  for minimal representations of a plane [12, 38] and  $13 \times 4$  for homogeneous coordinates of a plane [7]).

Now we consider the form of  $\mathbf{J}_{ij}$ . Let us define

$$\mathbf{C}_{ij} = \begin{bmatrix} \mathbf{c}_{ij1}^T \\ \mathbf{c}_{ij2}^T \\ \vdots \\ \mathbf{c}_{ijK_{ij}}^T \end{bmatrix}, \quad (19)$$

where the  $k$ th row  $\mathbf{c}_{ijk}^T$  is defined in (14).  $\mathbf{C}_{ij}$  is a matrix of size  $K_{ij} \times 13$ . Substituting (17) and (18) into (10) and using the definition of  $\mathbf{C}_{ij}$  in (19), we have

$$\begin{aligned} \mathbf{J}_{ij} &= \begin{bmatrix} \mathbf{0} & \dots & \mathbf{c}_{ij1}^T \mathbf{V}_{ij}^{\boldsymbol{\rho}_i} & \dots & \mathbf{0} & \dots & \mathbf{c}_{ij1}^T \mathbf{V}_{ij}^{\boldsymbol{\omega}_j} & \dots & \mathbf{0} \\ \mathbf{0} & \dots & \mathbf{c}_{ij2}^T \mathbf{V}_{ij}^{\boldsymbol{\rho}_i} & \dots & \mathbf{0} & \dots & \mathbf{c}_{ij2}^T \mathbf{V}_{ij}^{\boldsymbol{\omega}_j} & \dots & \mathbf{0} \\ \vdots & \ddots & \vdots & \ddots & \vdots & \ddots & \vdots & \ddots & \vdots \\ \mathbf{0} & \dots & \underbrace{\mathbf{c}_{ijK_{ij}}^T \mathbf{V}_{ij}^{\boldsymbol{\rho}_i}}_{\mathbf{C}_{ij} \mathbf{V}_{ij}^{\boldsymbol{\rho}_i}} & \dots & \mathbf{0} & \dots & \underbrace{\mathbf{c}_{ijK_{ij}}^T \mathbf{V}_{ij}^{\boldsymbol{\omega}_j}}_{\mathbf{C}_{ij} \mathbf{V}_{ij}^{\boldsymbol{\omega}_j}} & \dots & \mathbf{0} \end{bmatrix} \\ &= \begin{bmatrix} \mathbf{0} & \dots & \mathbf{C}_{ij} \mathbf{V}_{ij}^{\boldsymbol{\rho}_i} & \dots & \mathbf{0} & \dots & \mathbf{C}_{ij} \mathbf{V}_{ij}^{\boldsymbol{\omega}_j} & \dots & \mathbf{0} \end{bmatrix}. \end{aligned} \quad (20)$$

**Jacobian Matrix for the First Pose** Suppose  $\mathbb{P}_{1j}$  is the set of measurements from the  $j$ th plane  $\boldsymbol{\omega}_j$  at the first pose  $\boldsymbol{\rho}_1$ . As we fix  $\boldsymbol{\rho}_1$  during the optimization, the Jacobian matrix  $\mathbf{J}_{1j}$  derived from  $\mathbb{P}_{1j}$  has a special form as

$$\mathbf{J}_{1j} = \begin{bmatrix} \mathbf{0} & \dots & \mathbf{0} & \dots & \mathbf{0} & \dots & \mathbf{C}_{1j} \mathbf{V}_{1j}^{\boldsymbol{\omega}_j} & \dots & \mathbf{0} \end{bmatrix} \quad (21)$$

### 3.3 Factorization of $\mathbf{C}_{ij}$

$\mathbf{C}_{ij}$  has a special structure. It has duplicated columns, according to the structure of  $\mathbf{c}_{ijk}$  defined in (14). We have the following lemma about  $\mathbf{C}_{ij}$ :

**Lemma 1.**  $\mathbf{C}_{ij}$  can be written in the following form

$$\mathbf{C}_{ij} = \mathbf{Q}_{ij} \mathbf{M}_{ij}, \quad (22)$$

where  $\mathbf{M}_{ij}$  has the size  $4 \times 13$  and  $\mathbf{Q}_{ij}^T \mathbf{Q}_{ij} = \mathbf{I}_4$ , where  $\mathbf{I}_4$  is the  $4 \times 4$  identity matrix.

*Proof.* As shown in the definition of  $\mathbf{c}_{ijk}$  in (14),  $x_{ijk}$ ,  $y_{ijk}$ ,  $z_{ijk}$  and 1 are duplicated several times to form  $\mathbf{c}_{ijk}$ . Therefore, there are only 4 unique columns among the 13 columns of  $\mathbf{C}_{ij}$ , which contains the constant 1 and the  $x$ ,  $y$ ,  $z$  coordinates of points within  $\mathbb{P}_{ij}$ . We denote them as

$$\mathbf{E}_{ij} = \begin{bmatrix} x_{ij1} & y_{ij1} & z_{ij1} & 1 \\ x_{ij2} & y_{ij2} & z_{ij2} & 1 \\ \vdots & \vdots & \vdots & \vdots \\ \underbrace{x_{ijK_{ij}}}_{\mathbf{x}_{ij}} & \underbrace{y_{ijK_{ij}}}_{\mathbf{y}_{ij}} & \underbrace{z_{ijK_{ij}}}_{\mathbf{z}_{ij}} & \underbrace{1}_{\mathbf{1}} \end{bmatrix} = [\mathbf{x}_{ij} \quad \mathbf{y}_{ij} \quad \mathbf{z}_{ij} \quad \mathbf{1}]. \quad (23)$$

The 13 columns in  $\mathbf{C}_{ij}$  are simply copies of the 4 columns in  $\mathbf{E}_{ij}$ . Let us define the thin QR decomposition [4] of  $\mathbf{E}_{ij}$  as

$$\mathbf{E}_{ij} = \mathbf{Q}_{ij} \mathbf{U}_{ij} \quad (24)$$

where  $\mathbf{Q}_{ij}^T \mathbf{Q}_{ij} = \mathbf{I}_4$  and  $\mathbf{U}_{ij}$  is an upper triangular matrix.  $\mathbf{Q}_{ij}$  is of size  $K_{ij} \times 4$  and  $\mathbf{U}_{ij}$  is of size  $4 \times 4$ . Here we use the thin QR

decomposition, since the number of points  $K_{ij}$  is generally much larger than 4. The thin QR decomposition can reduce computational time. We partition  $\mathbf{U}_{ij}$  into its columns as

$$\mathbf{U}_{ij} = \begin{bmatrix} \mathbf{u}_{ij}^1 & \mathbf{u}_{ij}^2 & \mathbf{u}_{ij}^3 & \mathbf{u}_{ij}^4 \end{bmatrix}. \quad (25)$$

Substituting (25) into (23), we have

$$\mathbf{E}_{ij} = \mathbf{Q}_{ij} \begin{bmatrix} \mathbf{u}_{ij}^1 & \mathbf{u}_{ij}^2 & \mathbf{u}_{ij}^3 & \mathbf{u}_{ij}^4 \end{bmatrix} \quad (26)$$

Comparing (23) and (26), we get

$$\begin{aligned} \mathbf{x}_{ij} &= \mathbf{Q}_{ij} \mathbf{u}_{ij}^1, & \mathbf{y}_{ij} &= \mathbf{Q}_{ij} \mathbf{u}_{ij}^2, \\ \mathbf{z}_{ij} &= \mathbf{Q}_{ij} \mathbf{u}_{ij}^3, & \mathbf{1} &= \mathbf{Q}_{ij} \mathbf{u}_{ij}^4 \end{aligned} \quad (27)$$

As the columns of  $\mathbf{C}_{ij}$  are copies of the columns of  $\mathbf{E}_{ij}$ , according to the form of  $\mathbf{c}_{ijk}$  in (14) and the definition of  $\mathbf{E}_{ij}$  in (23),  $\mathbf{C}_{ij}$  can be written as

$$\mathbf{C}_{ij} = \begin{bmatrix} \mathbf{x}_{ij}, \mathbf{y}_{ij}, \mathbf{z}_{ij}, \mathbf{x}_{ij}, \mathbf{y}_{ij}, \mathbf{z}_{ij}, \mathbf{x}_{ij}, \mathbf{y}_{ij}, \mathbf{z}_{ij}, \mathbf{1}, \mathbf{1}, \mathbf{1}, \mathbf{1} \end{bmatrix} \quad (28)$$

Substituting (27) into (28), we finally have

$$\begin{aligned} \mathbf{C}_{ij} &= \mathbf{Q}_{ij} \underbrace{\begin{bmatrix} \mathbf{u}_{ij}^1, \mathbf{u}_{ij}^2, \mathbf{u}_{ij}^3, \mathbf{u}_{ij}^1, \mathbf{u}_{ij}^2, \mathbf{u}_{ij}^3, \mathbf{u}_{ij}^1, \mathbf{u}_{ij}^2, \mathbf{u}_{ij}^3, \mathbf{u}_{ij}^4, \mathbf{u}_{ij}^4, \mathbf{u}_{ij}^4 \end{bmatrix}}_{\mathbf{M}_{ij}} \\ &= \mathbf{Q}_{ij} \mathbf{M}_{ij} \end{aligned} \quad (29)$$

□

The factorization of  $\mathbf{C}_{ij}$  can be used to significantly reduce the computational cost as described below.

### 3.4 Reduced Jacobian Matrix

According to Lemma 1,  $\mathbf{C}_{ij}$  can be factorized as  $\mathbf{C}_{ij} = \mathbf{Q}_{ij} \mathbf{M}_{ij}$ . We define the **reduced Jacobian matrix**  $\mathbf{J}_{ij}^r$  of  $\mathbf{J}_{ij}$  as

$$\mathbf{J}_{ij}^r = \begin{cases} \begin{bmatrix} \mathbf{0} & \cdots & \mathbf{0} & \cdots & \mathbf{0} & \cdots & \mathbf{M}_{1j} \mathbf{V}_{1j}^{\omega_j} & \cdots & \mathbf{0} \end{bmatrix} & i = 1 \\ \begin{bmatrix} \mathbf{0} & \cdots & \mathbf{M}_{ij} \mathbf{V}_{ij}^{\rho_i} & \cdots & \mathbf{0} & \cdots & \mathbf{M}_{ij} \mathbf{V}_{ij}^{\omega_j} & \cdots & \mathbf{0} \end{bmatrix} & i \neq 1 \end{cases} \quad (30)$$

We call it a reduced Jacobian matrix, because  $\mathbf{M}_{ij}$  is a much smaller matrix than  $\mathbf{C}_{ij}$ .  $\mathbf{C}_{ij}$  has size  $K_{ij} \times 13$ . According to Lemma 1,  $\mathbf{M}_{ij}$  has size  $4 \times 13$ . Generally,  $K_{ij}$  is much larger than 4.

We stack  $\mathbf{J}_{ij}$  and  $\mathbf{J}_{ij}^r$  to form the Jacobian matrix  $\mathbf{J}$  and the reduced Jacobian matrix  $\mathbf{J}^r$  for the cost function (9), as

$$\mathbf{J} = \begin{bmatrix} \vdots \\ \mathbf{J}_{ij} \\ \vdots \end{bmatrix}, \quad \mathbf{J}^r = \begin{bmatrix} \vdots \\ \mathbf{J}_{ij}^r \\ \vdots \end{bmatrix}, \quad (31)$$

The following lemma shows that  $\mathbf{J}^r$  can replace  $\mathbf{J}$  to calculate  $\mathbf{J}^T \mathbf{J}$  in the LM algorithm.

**Lemma 2.** For the planar BA, we have  $\mathbf{J}^T \mathbf{J} = \mathbf{J}^{rT} \mathbf{J}^r$ .

*Proof.*  $\mathbf{J}$  and  $\mathbf{J}^r$  are block vectors in terms of  $\mathbf{J}_{ij}$  and  $\mathbf{J}_{ij}^r$  as defined in (31). According to block matrix multiplication, we have

$$\mathbf{J}^T \mathbf{J} = \sum_{i,j} \mathbf{J}_{ij}^T \mathbf{J}_{ij}, \quad \mathbf{J}^{rT} \mathbf{J}^r = \sum_{i,j} \mathbf{J}_{ij}^{rT} \mathbf{J}_{ij}^r \quad (32)$$

For  $i \neq 1$ , using the expression in (20),  $\mathbf{J}_{ij}^T \mathbf{J}_{ij}$  has the form

$$\mathbf{J}_{ij}^T \mathbf{J}_{ij} = \begin{bmatrix} \mathbf{0} & \cdots & \mathbf{0} & \cdots & \mathbf{0} & \cdots & \mathbf{0} \\ \vdots & & \vdots & & \vdots & & \vdots \\ \mathbf{0} & \cdots & \mathbf{V}_{ij}^{\rho_i T} \mathbf{C}_{ij}^T \mathbf{C}_{ij} \mathbf{V}_{ij}^{\rho_i} & \cdots & \mathbf{V}_{ij}^{\rho_i T} \mathbf{C}_{ij}^T \mathbf{C}_{ij} \mathbf{V}_{ij}^{\omega_j} & \cdots & \mathbf{0} \\ \vdots & & \vdots & & \vdots & & \vdots \\ \mathbf{0} & \cdots & \mathbf{V}_{ij}^{\omega_j T} \mathbf{C}_{ij}^T \mathbf{C}_{ij} \mathbf{V}_{ij}^{\rho_i} & \cdots & \mathbf{V}_{ij}^{\omega_j T} \mathbf{C}_{ij}^T \mathbf{C}_{ij} \mathbf{V}_{ij}^{\omega_j} & \cdots & \mathbf{0} \\ \vdots & & \vdots & & \vdots & & \vdots \\ \mathbf{0} & \cdots & \mathbf{0} & \cdots & \mathbf{0} & \cdots & \mathbf{0} \end{bmatrix} \quad (33)$$

Similarly, using the expression in (30),  $\mathbf{J}_{ij}^{rT} \mathbf{J}_{ij}^r$  has the form

$$\mathbf{J}_{ij}^{rT} \mathbf{J}_{ij}^r = \begin{bmatrix} \mathbf{0} & \cdots & \mathbf{0} & \cdots & \mathbf{0} & \cdots & \mathbf{0} \\ \vdots & & \vdots & & \vdots & & \vdots \\ \mathbf{0} & \cdots & \mathbf{V}_{ij}^{\rho_i T} \mathbf{M}_{ij}^T \mathbf{M}_{ij} \mathbf{V}_{ij}^{\rho_i} & \cdots & \mathbf{V}_{ij}^{\rho_i T} \mathbf{M}_{ij}^T \mathbf{M}_{ij} \mathbf{V}_{ij}^{\omega_j} & \cdots & \mathbf{0} \\ \vdots & & \vdots & & \vdots & & \vdots \\ \mathbf{0} & \cdots & \mathbf{V}_{ij}^{\omega_j T} \mathbf{M}_{ij}^T \mathbf{M}_{ij} \mathbf{V}_{ij}^{\rho_i} & \cdots & \mathbf{V}_{ij}^{\omega_j T} \mathbf{M}_{ij}^T \mathbf{M}_{ij} \mathbf{V}_{ij}^{\omega_j} & \cdots & \mathbf{0} \\ \vdots & & \vdots & & \vdots & & \vdots \\ \mathbf{0} & \cdots & \mathbf{0} & \cdots & \mathbf{0} & \cdots & \mathbf{0} \end{bmatrix} \quad (34)$$

Substituting (22) into  $\mathbf{V}_{ij}^T \mathbf{C}_{ij}^T \mathbf{C}_{ij} \mathbf{V}_{ij}$  and using the fact  $\mathbf{Q}_{ij}^T \mathbf{Q}_{ij} = \mathbf{I}_4$ , we have

$$\begin{aligned} \mathbf{V}_{ij}^{\rho_i T} \mathbf{C}_{ij}^T \mathbf{C}_{ij} \mathbf{V}_{ij}^{\rho_i} &= \mathbf{V}_{ij}^{\rho_i T} \mathbf{M}_{ij}^T (\mathbf{Q}_{ij}^T \mathbf{Q}_{ij}) \mathbf{M}_{ij} \mathbf{V}_{ij}^{\rho_i} \\ &= \mathbf{V}_{ij}^{\rho_i T} \mathbf{M}_{ij}^T \mathbf{M}_{ij} \mathbf{V}_{ij}^{\rho_i} \end{aligned} \quad (35)$$

Similarly, we have

$$\begin{aligned} \mathbf{V}_{ij}^{\rho_i T} \mathbf{C}_{ij}^T \mathbf{C}_{ij} \mathbf{V}_{ij}^{\omega_j} &= \mathbf{V}_{ij}^{\rho_i T} \mathbf{M}_{ij}^T \mathbf{M}_{ij} \mathbf{V}_{ij}^{\omega_j} \\ \mathbf{V}_{ij}^{\omega_j T} \mathbf{C}_{ij}^T \mathbf{C}_{ij} \mathbf{V}_{ij}^{\rho_i} &= \mathbf{V}_{ij}^{\omega_j T} \mathbf{M}_{ij}^T \mathbf{M}_{ij} \mathbf{V}_{ij}^{\rho_i} \\ \mathbf{V}_{ij}^{\omega_j T} \mathbf{C}_{ij}^T \mathbf{C}_{ij} \mathbf{V}_{ij}^{\omega_j} &= \mathbf{V}_{ij}^{\omega_j T} \mathbf{M}_{ij}^T \mathbf{M}_{ij} \mathbf{V}_{ij}^{\omega_j} \end{aligned} \quad (36)$$

For  $i = 1$ , according to (21), the only non-zero term for  $\mathbf{J}_{1j}^T \mathbf{J}_{1j}$  is  $\mathbf{V}_{1j}^{\omega_j T} \mathbf{C}_{1j}^T \mathbf{C}_{1j} \mathbf{V}_{1j}^{\omega_j}$ . On the other hand, according to (30),  $\mathbf{J}_{1j}^{rT} \mathbf{J}_{1j}^r$  has only one corresponding non-zero term  $\mathbf{V}_{1j}^{\omega_j T} \mathbf{M}_{1j}^T \mathbf{M}_{1j} \mathbf{V}_{1j}^{\omega_j}$ . Similar to the derivation in (35), we have

$$\mathbf{V}_{1j}^{\omega_j T} \mathbf{C}_{1j}^T \mathbf{C}_{1j} \mathbf{V}_{1j}^{\omega_j} = \mathbf{V}_{1j}^{\omega_j T} \mathbf{M}_{1j}^T \mathbf{M}_{1j} \mathbf{V}_{1j}^{\omega_j}. \quad (37)$$

In summary, using (35), (36) and (37), we have  $\mathbf{J}_{ij}^T \mathbf{J}_{ij} = \mathbf{J}_{ij}^{rT} \mathbf{J}_{ij}^r$ . According to (32), consequently we have  $\mathbf{J}^T \mathbf{J} = \mathbf{J}^{rT} \mathbf{J}^r$ . □

### 3.5 Reduced Residual Vector

Let us define the residual vector for the  $K_{ij}$  points in  $\mathbb{P}_{ij}$  as  $\boldsymbol{\delta}_{ij} = [\delta_{ij1}, \delta_{ij2}, \dots, \delta_{ijK_{ij}}]^T$ . According to (13) and (19),  $\boldsymbol{\delta}_{ij}$  can be written as

$$\boldsymbol{\delta}_{ij} = \mathbf{C}_{ij} \mathbf{v}_{ij}. \quad (38)$$

We define the **reduced residual vector**  $\boldsymbol{\delta}_{ij}^r$  of  $\boldsymbol{\delta}_{ij}$  as

$$\boldsymbol{\delta}_{ij}^r = \mathbf{M}_{ij} \mathbf{v}_{ij} \quad (39)$$

Stacking all  $\delta_{ij}$  and  $\delta_{ij}^r$ , we get the residual vector  $\delta$  and the reduced residual vector  $\delta^r$  as

$$\delta = \begin{bmatrix} \vdots \\ \delta_{ij} \\ \vdots \end{bmatrix}, \quad \delta^r = \begin{bmatrix} \vdots \\ \delta_{ij}^r \\ \vdots \end{bmatrix}. \quad (40)$$

The following lemma shows that  $\delta^r$  can replace  $\delta$  in the LM algorithm.

**Lemma 3.** *For the planar BA, we have  $\mathbf{J}^T \delta = \mathbf{J}^{rT} \delta^r$ .*

*Proof.*  $\mathbf{J}$ ,  $\mathbf{J}^r$ ,  $\delta$  and  $\delta^r$  are block vectors with elements  $\mathbf{J}_{ij}$ ,  $\mathbf{J}_{ij}^r$ ,  $\delta_{ij}$  and  $\delta_{ij}^r$  as defined in (31) and (40), respectively. Applying the block matrix multiplication, we have

$$\mathbf{J}^T \delta = \sum_{ij} \mathbf{J}_{ij}^T \delta_{ij}, \quad \mathbf{J}^{rT} \delta^r = \sum_{ij} \mathbf{J}_{ij}^{rT} \delta_{ij}^r \quad (41)$$

For  $i \neq 1$ , using the expression of  $\mathbf{J}_{ij}$  in (20) and  $\mathbf{J}_{ij}^r$  in (30), and the expression of  $\delta_{ij}$  in (38) and  $\delta_{ij}^r$  in (39),  $\mathbf{J}_{ij}^T \delta_{ij}$  and  $\mathbf{J}_{ij}^{rT} \delta_{ij}^r$  have the forms as

$$\mathbf{J}_{ij}^T \delta_{ij} = \begin{bmatrix} \mathbf{0} \\ \vdots \\ \mathbf{V}_{ij}^{\rho_i T} \mathbf{C}_{ij}^T \mathbf{C}_{ij} \mathbf{v}_{ij} \\ \vdots \\ \mathbf{V}_{ij}^{\omega_j T} \mathbf{C}_{ij}^T \mathbf{C}_{ij} \mathbf{v}_{ij} \\ \vdots \\ \mathbf{0} \end{bmatrix}, \quad \mathbf{J}_{ij}^{rT} \delta_{ij}^r = \begin{bmatrix} \mathbf{0} \\ \vdots \\ \mathbf{V}_{ij}^{\rho_i T} \mathbf{M}_{ij}^T \mathbf{M}_{ij} \mathbf{v}_{ij} \\ \vdots \\ \mathbf{V}_{ij}^{\omega_j T} \mathbf{M}_{ij}^T \mathbf{M}_{ij} \mathbf{v}_{ij} \\ \vdots \\ \mathbf{0} \end{bmatrix} \quad (42)$$

Substituting (22) into  $\mathbf{V}_{ij}^{\rho_i T} \mathbf{C}_{ij}^T \mathbf{C}_{ij} \mathbf{v}_{ij}$  and using the fact  $\mathbf{Q}_{ij}^T \mathbf{Q}_{ij} = \mathbf{I}_4$ , we have

$$\begin{aligned} \mathbf{V}_{ij}^{\rho_i T} \mathbf{C}_{ij}^T \mathbf{C}_{ij} \mathbf{v}_{ij} &= \mathbf{V}_{ij}^{\rho_i T} \mathbf{M}_{ij}^T (\mathbf{Q}_{ij}^T \mathbf{Q}_{ij}) \mathbf{M}_{ij} \mathbf{v}_{ij} \\ &= \mathbf{V}_{ij}^{\rho_i T} \mathbf{M}_{ij}^T \mathbf{M}_{ij} \mathbf{v}_{ij} \end{aligned} \quad (43)$$

Similarly, we have

$$\mathbf{V}_{ij}^{\omega_j T} \mathbf{C}_{ij}^T \mathbf{C}_{ij} \mathbf{v}_{ij} = \mathbf{V}_{ij}^{\omega_j T} \mathbf{M}_{ij}^T \mathbf{M}_{ij} \mathbf{v}_{ij} \quad (44)$$

For  $i = 1$ , substituting (21) and (38) into  $\mathbf{J}_{1j}^T \delta_{1j}$  and applying the block matrix multiplication, we find the only non-zero term of  $\mathbf{J}_{1j}^T \delta_{1j}$  is  $\mathbf{V}_{1j}^{\omega_j T} \mathbf{C}_{1j}^T \mathbf{C}_{1j} \mathbf{v}_{1j}$ . On the other hand, substituting (30) and (39) into  $\mathbf{J}_{1j}^{rT} \delta_{1j}^r$ , we find that  $\mathbf{J}_{1j}^{rT} \delta_{1j}^r$  only has one non-zero term  $\mathbf{V}_{1j}^{\omega_j T} \mathbf{M}_{1j}^T \mathbf{M}_{1j} \mathbf{v}_{1j}$ . Similar to the derivation in (43), we have

$$\mathbf{V}_{1j}^{\omega_j T} \mathbf{C}_{1j}^T \mathbf{C}_{1j} \mathbf{v}_{1j} = \mathbf{V}_{1j}^{\omega_j T} \mathbf{M}_{1j}^T \mathbf{M}_{1j} \mathbf{v}_{1j} \quad (45)$$

In summary, from (43), (44) and (45), we have  $\mathbf{J}_{ij}^T \delta_{ij} = \mathbf{J}_{ij}^{rT} \delta_{ij}^r$ . According to (41), we finally get  $\mathbf{J}^T \delta = \mathbf{J}^{rT} \delta^r$ .  $\square$

### 3.6 Planar Bundle Adjustment Algorithm

According to Lemma 1, Lemma 2 and Lemma 3, we have the following theorem.

**Theorem 1.** *For the planar BA,  $\mathbf{J}^r$  and  $\delta^r$  can replace  $\mathbf{J}$  and  $\delta$  in (5) to compute the step in the LM algorithm, and each block  $\mathbf{J}_{ij}^r$  and  $\delta_{ij}^r$  in  $\mathbf{J}^r$  and  $\delta^r$  has 4 rows.*

*Proof.* LM algorithm uses (5) to calculate the step for each iteration. According to Lemma 2, we have  $\mathbf{J}^T \mathbf{J} = \mathbf{J}^{rT} \mathbf{J}^r$ . Besides, based on Lemma 3, we have  $\mathbf{J}^T \delta = \mathbf{J}^{rT} \delta^r$ . Consequently, we have  $(\mathbf{J}^{rT} \mathbf{J}^r + \lambda \mathbf{I}) \xi = \mathbf{J}^{rT} \delta^r$  is equivalent to  $(\mathbf{J}^T \mathbf{J} + \lambda \mathbf{I}) \xi = \mathbf{J}^T \delta$ . Thus  $\mathbf{J}^r$  and  $\delta^r$  can replace  $\mathbf{J}$  and  $\delta$  for computing the step in the LM algorithm.

According to the definition of  $\mathbf{J}_{ij}^r$  in (30) and  $\delta_{ij}^r$  in (39), we know that the number of rows of  $\mathbf{J}_{ij}^r$  and  $\delta_{ij}^r$  is the same as the number of rows of  $\mathbf{M}_{ij}$ . According to Lemma 1,  $\mathbf{M}_{ij}$  has 4 rows. Consequently, we have that  $\mathbf{J}_{ij}^r$  and  $\delta_{ij}^r$  have 4 rows.  $\square$

As mentioned in Theorem 1, no matter how many points are in  $\mathbb{P}_{ij}$ , the reduced  $\mathbf{J}_{ij}^r$  and  $\delta_{ij}^r$  always have 4 rows. This significantly reduces the computational cost in the LM algorithm. Specifically, we have the following corollary:

**Corollary 1.1.** *The runtime for computing  $\mathbf{J}_{ij}^r$ ,  $\delta_{ij}^r$ ,  $\mathbf{J}_{ij}^{rT} \mathbf{J}_{ij}^r$  and  $\mathbf{J}_{ij}^{rT} \delta_{ij}^r$  is  $\frac{4}{K_{ij}}$  relative to computing the original  $\mathbf{J}_{ij}$ ,  $\delta_{ij}$ ,  $\mathbf{J}_{ij}^T \mathbf{J}_{ij}$  and  $\mathbf{J}_{ij}^T \delta_{ij}$ , respectively.*

*Proof.* From the expressions for  $\mathbf{J}_{ij}^r$  in (30) and  $\mathbf{J}_{ij}$  in (10) and (21), we know that the difference between  $\mathbf{J}_{ij}^r$  and  $\mathbf{J}_{ij}$  is that we use  $\mathbf{M}_{ij}$  to replace  $\mathbf{C}_{ij}$ .  $\mathbf{M}_{ij}$  has 4 rows and  $\mathbf{C}_{ij}$  has  $K_{ij}$  rows. Thus, the runtime for computing  $\mathbf{J}_{ij}^r$  is  $\frac{4}{K_{ij}}$  relative to computing  $\mathbf{J}_{ij}$ . Similarly, the runtime for computing  $\delta_{ij}^r$  is  $\frac{4}{K_{ij}}$  relative to computing  $\delta_{ij}$ .

According to Theorem 1,  $\mathbf{J}_{ij}^r$  and  $\delta_{ij}^r$  each has 4 rows, and  $\mathbf{J}_{ij}$  and  $\delta_{ij}$  each has  $K_{ij}$  rows. According to the rules of matrix multiplication, the runtime for computing  $\mathbf{J}_{ij}^{rT} \mathbf{J}_{ij}^r$  and  $\mathbf{J}_{ij}^{rT} \delta_{ij}^r$  is  $\frac{4}{K_{ij}}$  relative to computing  $\mathbf{J}_{ij}^T \mathbf{J}_{ij}$  and  $\mathbf{J}_{ij}^T \delta_{ij}$ , respectively.  $\square$

The additional cost here is to calculate  $\mathbf{C}_{ij} = \mathbf{Q}_{ij} \mathbf{M}_{ij}$ . As  $\mathbf{C}_{ij}$  keeps constant during the iteration, we only need to compute it once before the iteration. As shown in our experimental results, this step only slightly increases the computational time for the pose graph initialization step. We summarize our PBA in Algorithm 1.

---

#### Algorithm 1: Planar Bundle Adjustment

---

**Input:** Initial guess of  $N - 1$  poses and  $M$  plane parameters, and the measurements  $\{\mathbb{P}_{ij}\}$ .

**Result:** Refined poses and plane parameters.

// Initialization

- 1 Calculate  $\mathbf{c}_{ijk}$  for each  $\mathbf{p}_{ijk} \in \mathbb{P}_{ij}$  as (14);
- 2 Stack  $\mathbf{c}_{ijk}$  to get  $\mathbf{C}_{ij}$  as (19);
- 3 Compute the factorization  $\mathbf{C}_{ij} = \mathbf{Q}_{ij} \mathbf{M}_{ij}$  as mentioned in Lemma 1;

// Iterative Refine

- 4 **while not converge do**
  - 5     Compute the reduced Jacobian matrix block  $\mathbf{J}_{ij}^r$  in (30) and the reduced residual block  $\delta_{ij}^r$  in (39);
  - 6     Stack them to form  $\mathbf{J}^r$  and  $\delta^r$ ;
  - 7     Use the LM algorithm to update current estimate;
  - 8 **end**
- 

**Combine Planes with Other Features** Planes are sometimes together with other features, such as points [5, 18, 31, 34, 38]. In the cost function derived from multiple features, the Jacobian matrix from the plane cost would have the same form as (20) and (21), and the residual vector would also have the same form as (38). Therefore, they can be replaced by our reduced Jacobian matrix and reduced residual vector in the BA with multiple features.

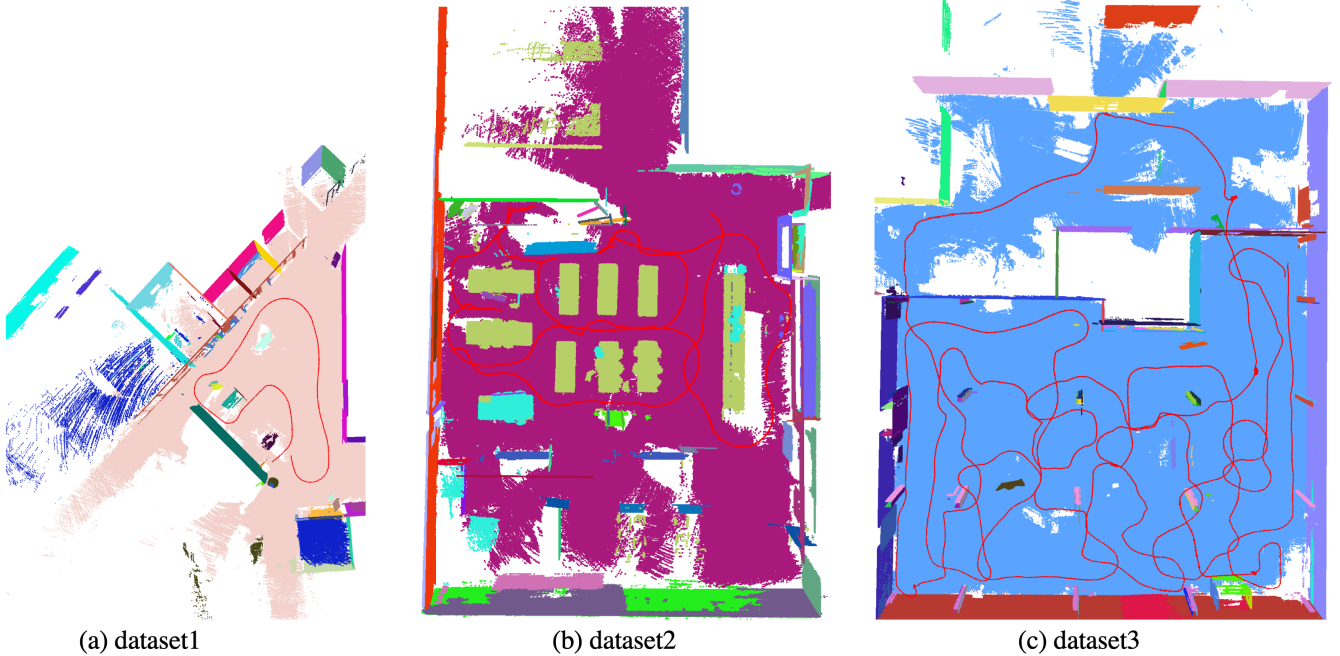


Figure 4: The three datasets used in our experiments.

Table 1: The characteristics of the 3 datasets.

dataset	#poses	#planes	#points	length (m)
dataset1	695	154	$6.98 \times 10^6$	43.2
dataset2	1781	370	$16.82 \times 10^6$	104.4
dataset3	6547	591	$68.99 \times 10^6$	403.5

## 4 EXPERIMENTS

In this section, we evaluate the performance of our algorithm. We compare our algorithm against the direct solution for the point-to-plane cost (9) using the traditional BA framework (**DPT2PL**), and the state-of-the-art solution [3] using plane-to-plane cost (**PL2PL**). We evaluate the accuracy, computational time, convergence speed and the robustness to errors of the initialization in the compared algorithms.

**Datasets** We collected 3 indoor datasets using the NavVis M6 device<sup>1</sup>. The NavVis M6 estimates the device pose using 1 multi-layer Velodyne LiDAR, 3 single-layer LiDAR, IMU, WiFi signals as well as ground control points. It provides an accurate trajectory and a dense point cloud with an accuracy on the order of centimeters. We use the recordings of the Velodyne LiDAR<sup>2</sup> and the trajectory from the NavVis M6 to build the datasets. We sampled the trajectory so that the distance between two poses is larger than  $5cm$ . Planes are detected for each recording of the Velodyne LiDAR by the region-growing method introduced in [26]. Then we use the known pose to get the plane-plane data association. Specifically, the global planes are initialized by the planes detected in the first pose. We track and grow the global planes frame by frame. Local planes of the latest frame are first transformed into the global coordinate system using the known pose. We calculate the distances between points of a local plane and each of the global planes, and then we select the global plane that has the shortest mean point-to-plane distance. A match occurs when a local plane and the closest global plane have a mean

point-to-plane distance smaller than  $5cm$ , and the angle between the normals of the two planes is less than  $10^\circ$ . The points of the local plane whose distances are less than  $5cm$  are then added into the global plane, and the parameters of the global plane are then updated. Unmatched local planes that have more than 50 points are recognized as new planes, and are added into the global plane list for tracking during future frames. Fig. 4 shows the 3 datasets. The characteristics of the 3 datasets are listed in Table 1.

**Initialization Error** The LM algorithm requires an initial set of values for the unknowns. We consider how the error in the initial estimation affects the performance of the different algorithms. Specifically, we perturb the rotation matrix by an error rotation matrix represented by the Euler angles which are sampled from a zero-mean Gaussian distribution with standard deviation (STD)  $\delta_{\mathbf{R}}$ . Additionally, we add zero-mean Gaussian noise with STD  $\delta_{\mathbf{t}}$  to the translation. We add noise to the trajectory as follows. To simplify the notation, we use  $\mathbf{T} = \begin{bmatrix} \mathbf{R} & \mathbf{t} \\ \mathbf{0} & 1 \end{bmatrix}$  to represent a rigid transformation.

We first consider adding noise to two consecutive poses  $\mathbf{T}_i$  and  $\mathbf{T}_{i+1}$ . Assume  $\mathbf{T}_i^{i+1}$  is the relative pose between  $\mathbf{T}_i$  and  $\mathbf{T}_{i+1}$ , and  $\hat{\mathbf{T}}_i$  and  $\hat{\mathbf{T}}_{i+1}$  are the perturbed poses, respectively. We perturb  $\mathbf{T}_i$  and  $\mathbf{T}_{i+1}$  by  $\mathbf{T}_i^{err}$  and  $\mathbf{T}_{i+1}^{err}$ , respectively, so that  $\hat{\mathbf{T}}_i = \mathbf{T}_i^{err} \mathbf{T}_i$  and  $\hat{\mathbf{T}}_{i+1} = \mathbf{T}_{i+1}^{err} \mathbf{T}_i^{i+1} \hat{\mathbf{T}}_i$ . It is clear that the noise  $\mathbf{T}_i^{err}$  on  $\mathbf{T}_i$  will also affect  $\mathbf{T}_{i+1}$ . We start this process from  $i = 1$ . Thus, the noise will accumulate along the trajectory. We consider three noise levels as listed below:

- Noise Level 1:  $\delta_{\mathbf{R}} = 0.1^\circ$ ,  $\delta_{\mathbf{t}} = 0.01m$
- Noise Level 2:  $\delta_{\mathbf{R}} = 0.5^\circ$ ,  $\delta_{\mathbf{t}} = 0.03m$
- Noise Level 3:  $\delta_{\mathbf{R}} = 1.0^\circ$ ,  $\delta_{\mathbf{t}} = 0.05m$

Although the noise is small in terms of one pose, the noise accumulating along the trajectory may yield a large error. Generally, a longer trajectory will lead to a larger error. Fig. 5 shows the perturbed as well as the original trajectories for the 3 datasets. We use

<sup>1</sup><https://www.navvis.com/m6>

<sup>2</sup><https://velodynelidar.com/>

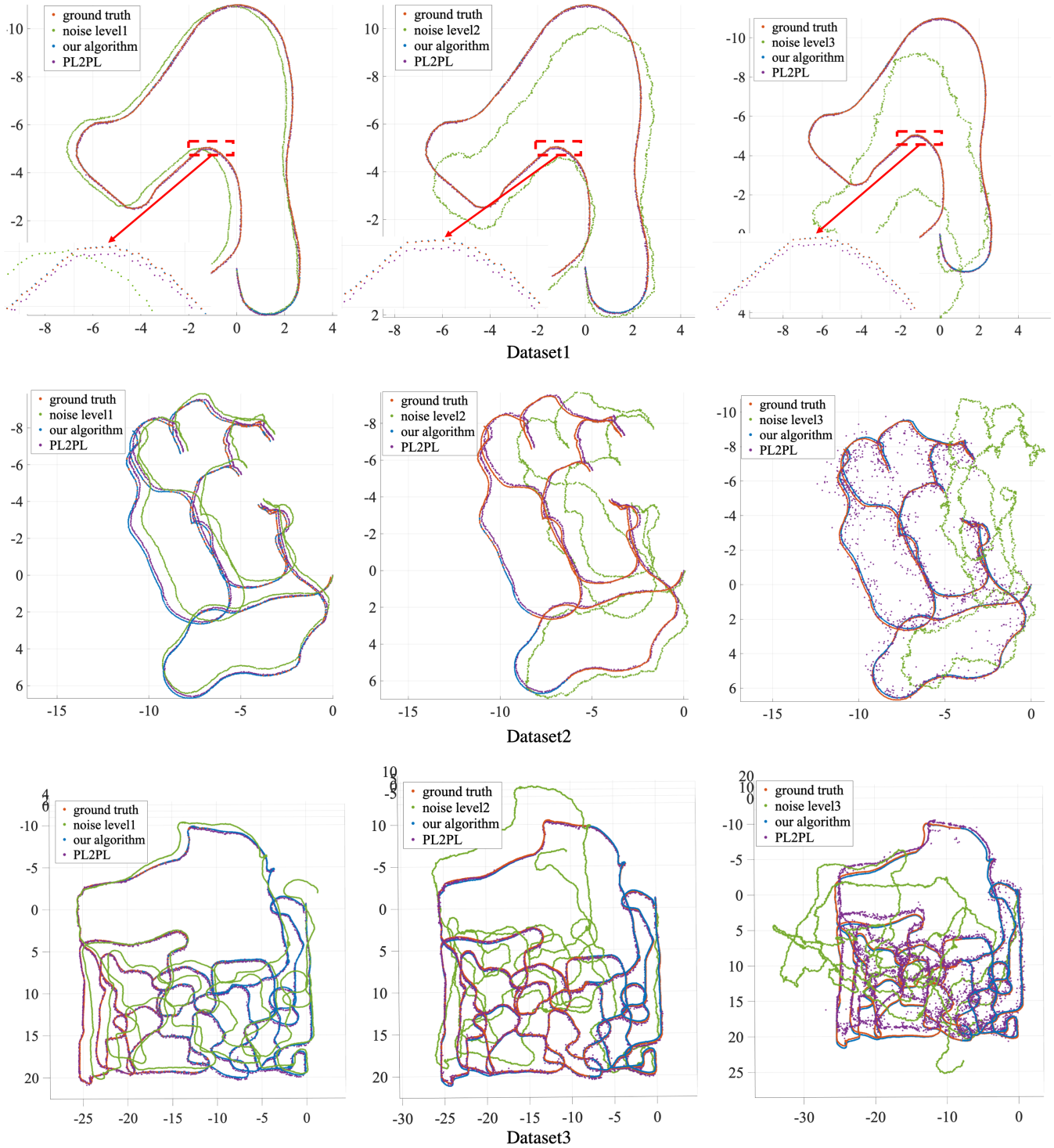


Figure 5: Experimental results of our algorithm and PL2PL [3] with varying initialization noise levels. PL2PL is not stable to large initial errors.

the perturbed trajectory to initialize the poses. For planes, we first calculate their local parameters from the local point clouds at the first poses that observe them. We initialize the global plane parameters by transforming the local parameters into the global coordinate system using the perturbed poses.

**Experiment Setup** In the experiments, all algorithms use the

same parameterizations for the rotation matrix and the plane, *i.e.*, angle-axis and CP parameterization [3], respectively. We ran the experiments on a computer with an Intel(R) Xeon(R) E5-2620 2.10GHz CPU and 80G memory. We adopted Ceres [1] as the non-linear least-squares solver, and used the Schur complement trick [33] to solve the linear system (6) (specifically, SPARSE.SCHUR linear



Table 2: Experimental results for different algorithms. The column QR shows the time for the QR decomposition of our algorithm. The column Init. presents the time for initializing the Ceres solver. The column Optimization describes the total time for the LM algorithm. The column Per Iter. lists the average runtime for each LM iteration. Our algorithm has a lower initialization time. The computational cost for QR decomposition is ignorable compared to the significant gain from the optimization process. Specifically, our algorithm is about 74, 49 and 107 times faster than DPT2PL on the three datasets, respectively. Here we only evaluate DPT2PL on Noise Level 1 for the 3 datasets, as we only consider the computational time of DPT2PL. For a specific dataset, the runtime of one iteration for different noise levels is similar. Our algorithm is more accurate, has lower computational complexity and converges faster than PL2PL [3].

Dataset	Noise Level	Method	#Iter	ATE		Cost in Eq. (9)		Time (s)			
				ATE <sub>R</sub> (°)	ATE <sub>t</sub> (m)	Initial	Final	QR	Init.	Optimization	Per Iter.
dataset1	level 1	Ours	81	$4.44 \times 10^{-2}$	$3.07 \times 10^{-4}$	$2.38 \times 10^5$	$1.42 \times 10^3$	1.16	0.016	11.06	0.14
		DPT2PL	81	$4.44 \times 10^{-2}$	$3.07 \times 10^{-4}$	$2.38 \times 10^5$	$1.42 \times 10^3$	0	6.26	823.31	10.16
		PL2PL [3]	384	0.58	0.28	$2.38 \times 10^5$	$1.98 \times 10^4$	0	0.026	69.53	0.18
	level 2	Ours	176	$4.68 \times 10^{-2}$	$3.98 \times 10^{-4}$	$1.78 \times 10^6$	$1.42 \times 10^3$	1.18	0.017	22.86	0.13
		PL2PL [3]	1000	0.58	0.28	$1.78 \times 10^6$	$1.98 \times 10^4$	0	0.025	185.97	0.19
	level 3	Ours	224	$4.96 \times 10^{-2}$	$4.22 \times 10^{-4}$	$1.78 \times 10^6$	$1.42 \times 10^3$	1.15	0.016	28.56	0.13
PL2PL [3]		1000	0.58	0.28	$1.78 \times 10^6$	$1.98 \times 10^4$	0	0.024	165.64	0.17	
dataset2	level 1	Ours	75	$4.88 \times 10^{-2}$	$8.57 \times 10^{-5}$	$7.27 \times 10^5$	$3.88 \times 10^3$	2.88	0.060	37.90	0.51
		DPT2PL	75	$4.88 \times 10^{-2}$	$8.57 \times 10^{-5}$	$7.27 \times 10^5$	$3.88 \times 10^3$	0	16.46	1843.87	24.58
		PL2PL [3]	203	0.95	0.16	$7.27 \times 10^5$	$8.46 \times 10^3$	0	0.11	219.45	1.08
	level 2	Ours	119	$5.76 \times 10^{-2}$	$2.32 \times 10^{-4}$	$4.38 \times 10^7$	$3.90 \times 10^3$	2.89	0.068	63.62	0.53
		PL2PL [3]	384	1.09	0.20	$4.38 \times 10^7$	$1.35 \times 10^4$	0	0.11	413.91	1.07
	level 3	Ours	723	$7.61 \times 10^{-2}$	$1.02 \times 10^{-2}$	$8.38 \times 10^7$	$4.23 \times 10^3$	2.86	0.062	365.70	0.51
PL2PL [3]		186	2.56	0.97	$8.38 \times 10^7$	$1.32 \times 10^6$	0	0.12	195.56	1.05	
dataset3	level 1	Ours	503	$4.28 \times 10^{-2}$	$3.17 \times 10^{-4}$	$2.81 \times 10^7$	$1.28 \times 10^4$	11.14	0.17	$4.87 \times 10^2$	0.97
		DPT2PL	503	$4.28 \times 10^{-2}$	$3.17 \times 10^{-4}$	$2.81 \times 10^7$	$1.28 \times 10^4$	0	77.03	$5.22 \times 10^4$	103.69
		PL2PL [3]	1000	0.90	0.41	$2.81 \times 10^7$	$4.00 \times 10^5$	0	0.35	$2.45 \times 10^3$	2.45
	level 2	Ours	883	$6.56 \times 10^{-2}$	$2.32 \times 10^{-2}$	$5.99 \times 10^8$	$1.39 \times 10^4$	10.89	0.16	$8.38 \times 10^2$	0.95
		PL2PL [3]	1000	0.95	0.47	$5.99 \times 10^8$	$7.02 \times 10^5$	0	0.36	$2.49 \times 10^3$	2.49
	level 3	Ours	13,385	$8.85 \times 10^{-2}$	$6.22 \times 10^{-2}$	$3.97 \times 10^9$	$1.40 \times 10^4$	11.32	0.17	$1.42 \times 10^4$	1.06
PL2PL [3]		15,000	8.66	1.34	$3.97 \times 10^9$	$1.02 \times 10^7$	0	0.33	$3.77 \times 10^4$	2.51	

solver in Ceres). We set the function and parameter tolerance to  $10^{-10}$ , and set the maximum number of iterations to 1000, except for the dataset3 at noise level 3. In this case, the initial error is very large, and more iterations are required. We set the maximum number of iterations to 15,000 for dataset3 at noise level 3.

We use the perturbed trajectory to initialize the LM algorithm, and compare the original trajectory with the results from the LM algorithm. We employ the absolute trajectory error (ATE) [42] to quantify the accuracy of the result. Specifically, for the  $k$ th pose, given the ground truth  $\mathbf{R}_k$  and  $\mathbf{t}_k$  and the estimation  $\hat{\mathbf{R}}_k$  and  $\hat{\mathbf{t}}_k$ , we calculate  $\Delta\mathbf{R}_k$  and  $\Delta\mathbf{t}_k$  as

$$\Delta\mathbf{R}_k = \mathbf{R}_k \hat{\mathbf{R}}_k^T, \quad \Delta\mathbf{t}_k = \mathbf{t}_k - \Delta\mathbf{R}_k \hat{\mathbf{t}}_k. \quad (46)$$

The ATE is calculated as

$$\text{ATE}_R = \left( \frac{1}{N} \sum_{k=1}^N \|\angle(\Delta\mathbf{R}_k)\|^2 \right)^{\frac{1}{2}}, \quad \text{ATE}_t = \left( \frac{1}{N} \sum_{k=1}^N \|\Delta\mathbf{t}_k\|^2 \right)^{\frac{1}{2}}, \quad (47)$$

where  $\angle(\cdot)$  is the angle of the angle-axis representation of  $\Delta\mathbf{R}_k$ .

**Results** It is clear that our algorithm is more accurate and more robust to the initialization error than PL2PL [3]. PL2PL converges with a smaller number of iterations (186 iterations) than our algorithm (723 iterations) for dataset2 at noise level 3. However, PL2PL probably converges to a local minimum, as PL2PL generates bad results for this input, as shown in Fig. 5. Except for this case, our algorithm converges faster. In addition, our algorithm has lower computational complexity than PL2PL [3]. One point-to-plane cost in (9) only involves 2 variables. But one relative plane cost in [3] involves 3 variables (2 poses and 1 plane). Thus the Jacobian matrix of [3] has more non-zero items than our reduced Jacobian matrix. This increases the runtime for calculating the Jacobian matrix  $\mathbf{J}$ ,  $\mathbf{J}^T \mathbf{J}$  and  $\mathbf{J}^T \boldsymbol{\delta}$ . For each iteration, our algorithm is more than 2 times

faster than [3] on dataset2 and dataset3. In the minimization process, our algorithm is about 74, 49 and 107 times faster than DPT2PL on the three datasets, respectively. The extra computational cost for the factorization  $\mathbf{C}_{ij} = \mathbf{Q}_{ij} \mathbf{M}_{ij}$  in (22) is marginal compared to the significant gain from the optimization process.

## 5 CONCLUSION

In this paper, we have studied the PBA problem. Our main contribution is to present an efficient solution for the PBA problem using the point-to-plane cost. Although the point-to-plane cost involves a large number of constraints, we find the resulting least-squares problem has special structure. We prove that we can use a reduced Jacobian matrix and residual vector with 4 rows to replace the original Jacobian matrix and residual vector with  $K_{ij}$  rows in the LM algorithm. This reduces the runtime for computing  $\mathbf{J}_{ij}$ ,  $\boldsymbol{\delta}_{ij}$ ,  $\mathbf{J}_{ij}^T \mathbf{J}_{ij}$  and  $\mathbf{J}_{ij}^T \boldsymbol{\delta}_{ij}$  by a factor of  $\frac{4}{K_{ij}}$  relative to the brute-force implementation. Our experimental results show that the extra cost of the one-time factorization is marginal compared to the significant gain from this new formulation. Furthermore, we have verified that our algorithm is faster, more accurate, and more robust to initial errors compared to the start-of-the-art formulation using the plane-to-plane cost for joint poses and planes optimization [3].

## REFERENCES

- [1] S. Agarwal, K. Mierle, and Others. Ceres solver. <http://ceres-solver.org>.
- [2] S. Agarwal, N. Snavely, S. M. Seitz, and R. Szeliski. Bundle adjustment in the large. In *European conference on computer vision*, pp. 29–42. Springer, 2010.
- [3] P. Geneva, K. Eickenhoff, Y. Yang, and G. Huang. LIPS: Lidar-inertial 3d plane SLAM. In *2018 IEEE/RSJ International Conference on Intelligent Robots and Systems (IROS)*, pp. 123–130. IEEE, 2018.
- [4] G. H. Golub and C. F. Van Loan. *Matrix computations*, vol. 3. JHU press, 2012.

- [5] W. S. Grant, R. C. Voorhies, and L. Itti. Efficient velodyne SLAM with point and plane features. *Autonomous Robots*, 43(5):1207–1224, 2019.
- [6] G. Grisetti, R. Kummerle, C. Stachniss, and W. Burgard. A tutorial on graph-based SLAM. *IEEE Intelligent Transportation Systems Magazine*, 2(4):31–43, 2010.
- [7] R. Hartley and A. Zisserman. *Multiple view geometry in computer vision*. Cambridge university press, 2003.
- [8] M. Hosseinzadeh, Y. Latif, T. Pham, N. Suenderhauf, and I. Reid. Structure aware SLAM using quadrics and planes. In *Asian Conference on Computer Vision*, pp. 410–426. Springer, 2018.
- [9] M. Hsiao, E. Westman, and M. Kaess. Dense planar-inertial SLAM with structural constraints. In *2018 IEEE International Conference on Robotics and Automation (ICRA)*, pp. 6521–6528. IEEE, 2018.
- [10] M. Hsiao, E. Westman, G. Zhang, and M. Kaess. Keyframe-based dense planar SLAM. In *2017 IEEE International Conference on Robotics and Automation (ICRA)*, pp. 5110–5117. IEEE, 2017.
- [11] N. Huang, J. Chen, and Y. Miao. Optimization for rgb-d SLAM based on plane geometrical constraint. In *2019 IEEE International Symposium on Mixed and Augmented Reality Adjunct (ISMAR-Adjunct)*, pp. 326–331. IEEE, 2019.
- [12] M. Kaess. Simultaneous localization and mapping with infinite planes. In *2015 IEEE International Conference on Robotics and Automation (ICRA)*, pp. 4605–4611. IEEE, 2015.
- [13] M. Kaess, H. Johannsson, R. Roberts, V. Ila, J. J. Leonard, and F. Deblaert. isam2: Incremental smoothing and mapping using the bayes tree. *The International Journal of Robotics Research*, 31(2):216–235, 2012.
- [14] P. Kim, B. Coltin, and H. Jin Kim. Linear rgb-d SLAM for planar environments. In *Proceedings of the European Conference on Computer Vision (ECCV)*, pp. 333–348, 2018.
- [15] G. Klein and D. W. Murray. Parallel tracking and mapping on a camera phone. *2009 8th IEEE International Symposium on Mixed and Augmented Reality*, pp. 83–86, 2009.
- [16] T. Lee, S. Lim, S. Lee, S. An, and S. Oh. Indoor mapping using planes extracted from noisy rgb-d sensors. In *2012 IEEE/RSJ International Conference on Intelligent Robots and Systems*, pp. 1727–1733, 2012.
- [17] K. Levenberg. A method for the solution of certain non-linear problems in least squares. *Quarterly of applied mathematics*, 2(2):164–168, 1944.
- [18] J. Li, B. Yang, K. Huang, G. Zhang, and H. Bao. Robust and efficient visual-inertial odometry with multi-plane priors. In *Chinese Conference on Pattern Recognition and Computer Vision (PRCV)*, pp. 283–295. Springer, 2019.
- [19] H. Liu, M. Chen, G. Zhang, H. Bao, and Y. Bao. ICE-BA: Incremental, consistent and efficient bundle adjustment for visual-inertial SLAM. In *Proceedings of the IEEE Conference on Computer Vision and Pattern Recognition*, pp. 1974–1982, 2018.
- [20] H. Liu, G. Zhang, and H. Bao. Robust keyframe-based monocular SLAM for augmented reality. In *2016 IEEE International Symposium on Mixed and Augmented Reality (ISMAR)*, pp. 1–10. IEEE, 2016.
- [21] M. I. Lourakis and A. A. Argyros. Sba: A software package for generic sparse bundle adjustment. *ACM Transactions on Mathematical Software (TOMS)*, 36(1):1–30, 2009.
- [22] J. J. Moré. The levenberg-marquardt algorithm: implementation and theory. In *Numerical analysis*, pp. 105–116. Springer, 1978.
- [23] R. Mur-Artal and J. D. Tardós. ORB-SLAM2: An open-source SLAM system for monocular, stereo, and rgb-d cameras. *IEEE Transactions on Robotics*, 33(5):1255–1262, 2017.
- [24] R. A. Newcombe, S. Izadi, O. Hilliges, D. Molyneaux, D. Kim, A. J. Davison, P. Kohi, J. Shotton, S. Hodges, and A. Fitzgibbon. Kinectfusion: Real-time dense surface mapping and tracking. In *2011 10th IEEE International Symposium on Mixed and Augmented Reality*, pp. 127–136. IEEE, 2011.
- [25] K. Pathak, A. Birk, N. Vaskevicius, and J. Poppinga. Fast registration based on noisy planes with unknown correspondences for 3-d mapping. *IEEE Transactions on Robotics*, 26(3):424–441, 2010.
- [26] J. Poppinga, N. Vaskevicius, A. Birk, and K. Pathak. Fast plane detection and polygonalization in noisy 3d range images. In *2008 IEEE/RSJ International Conference on Intelligent Robots and Systems*, pp. 3378–3383. IEEE, 2008.
- [27] C. R. Qi, H. Su, K. Mo, and L. J. Guibas. Pointnet: Deep learning on point sets for 3d classification and segmentation. In *Proceedings of the IEEE conference on computer vision and pattern recognition*, pp. 652–660, 2017.
- [28] R. F. Salas-Moreno, B. Glocker, P. H. Kelly, and A. J. Davison. Dense planar SLAM. In *2014 IEEE international symposium on mixed and augmented reality (ISMAR)*, pp. 157–164. IEEE, 2014.
- [29] J. L. Schonberger and J.-M. Frahm. Structure-from-Motion revisited. In *Proceedings of the IEEE Conference on Computer Vision and Pattern Recognition*, pp. 4104–4113, 2016.
- [30] T. Schöps, J. Engel, and D. Cremers. Semi-dense visual odometry for ar on a smartphone. In *2014 IEEE international symposium on mixed and augmented reality (ISMAR)*, pp. 145–150. IEEE, 2014.
- [31] Y. Taguchi, Y.-D. Jian, S. Ramalingam, and C. Feng. Point-plane SLAM for hand-held 3d sensors. In *2013 IEEE international conference on robotics and automation*, pp. 5182–5189. IEEE, 2013.
- [32] A. J. Trevor, J. G. Rogers, and H. I. Christensen. Planar surface SLAM with 3d and 2d sensors. In *2012 IEEE International Conference on Robotics and Automation*, pp. 3041–3048. IEEE, 2012.
- [33] B. Triggs, P. F. McLauchlan, R. I. Hartley, and A. W. Fitzgibbon. Bundle adjustment: a modern synthesis. In *International workshop on vision algorithms*, pp. 298–372. Springer, 1999.
- [34] J. Wang, J. Song, L. Zhao, S. Huang, and R. Xiong. A submap joining algorithm for 3d reconstruction using an rgb-d camera based on point and plane features. *Robotics and Autonomous Systems*, 118:93–111, 2019.
- [35] C. Wu, S. Agarwal, B. Curless, and S. M. Seitz. Multicore bundle adjustment. In *CVPR 2011*, pp. 3057–3064. IEEE, 2011.
- [36] S. Yang and S. Scherer. Monocular object and plane SLAM in structured environments. *IEEE Robotics and Automation Letters*, 4(4):3145–3152, 2019.
- [37] S. Yang, Y. Song, M. Kaess, and S. Scherer. Pop-up SLAM: Semantic monocular plane SLAM for low-texture environments. In *2016 IEEE/RSJ International Conference on Intelligent Robots and Systems (IROS)*, pp. 1222–1229. IEEE, 2016.
- [38] Y. Yang, P. Geneva, X. Zuo, K. Eickenhoff, Y. Liu, and G. Huang. Tightly-coupled aided inertial navigation with point and plane features. In *2019 International Conference on Robotics and Automation (ICRA)*, pp. 6094–6100. IEEE, 2019.
- [39] C. Zach. Robust bundle adjustment revisited. In *European Conference on Computer Vision*, pp. 772–787. Springer, 2014.
- [40] J. Zhang and S. Singh. Low-drift and real-time lidar odometry and mapping. *Autonomous Robots*, 41(2):401–416, 2017.
- [41] R. Zhang, S. Zhu, T. Fang, and L. Quan. Distributed very large scale bundle adjustment by global camera consensus. In *Proceedings of the IEEE International Conference on Computer Vision*, pp. 29–38, 2017.
- [42] Z. Zhang and D. Scaramuzza. A tutorial on quantitative trajectory evaluation for visual (-inertial) odometry. In *2018 IEEE/RSJ International Conference on Intelligent Robots and Systems (IROS)*, pp. 7244–7251. IEEE, 2018.
- [43] L. Zhou, S. Wang, and M. Kaess. A fast and accurate solution for pose estimation from 3D correspondences. In *2020 IEEE International Conference on Robotics and Automation (ICRA)*, 2020.